Concurrent Asian monsoon strengthening and early modern human dispersal to East Asia during the last interglacial

Hong Ao[a,b,1] (ORCID), Jiaoyang Ruan[c,d,1] (ORCID), María Martinón-Torres[e,f] (ORCID), Mario Krapp[g] (ORCID), Diederik Liebrand[h] (ORCID), Mark J. Dekkers[i] (ORCID), Thibaut Caley[j] (ORCID), Tara N. Jonell[k], Zongmin Zhu[l], Chunju Huang[l] (ORCID), Xinxia Li[a], Ziyun Zhang[a], Qiang Sun[m], Pingguo Yang[n], Jiali Jiang[l], Xinzhou Li[a] (ORCID), Xiaoxun Xie[a], Yougui Song[a] (ORCID), Xiaoke Qiang[a], Peng Zhang[a,b] (ORCID), and Zhisheng An[a,o,p] (ORCID)

The relationship between initial *Homo sapiens* dispersal from Africa to East Asia and the orbitally paced evolution of the Asian summer monsoon (ASM)—currently the largest monsoon system—remains underexplored due to lack of coordinated synthesis of both Asian paleoanthropological and paleoclimatic data. Here, we investigate orbital-scale ASM dynamics during the last 280 thousand years (kyr) and their likely influences on early *H. sapiens* dispersal to East Asia, through a unique integration of i) new centennial-resolution ASM records from the Chinese Loess Plateau, ii) model-based East Asian hydroclimatic reconstructions, iii) paleoanthropological data compilations, and iv) global *H. sapiens* habitat suitability simulations. Our combined proxy- and model-based reconstructions suggest that ASM precipitation responded to a combination of Northern Hemisphere ice volume, greenhouse gas, and regional summer insolation forcing, with cooccurring primary orbital cycles of ~100-kyr, 41-kyr, and ~20-kyr. Between ~125 and 70 kyr ago, summer monsoon rains and temperatures increased in vast areas across Asia. This episode coincides with the earliest *H. sapiens* fossil occurrence at multiple localities in East Asia. Following the transcontinental increase in simulated habitat suitability, we suggest that ASM strengthening together with Southeast African climate deterioration may have promoted the initial *H. sapiens* dispersal from their African homeland to remote East Asia during the last interglacial.

Asian monsoon | paleoclimate | loess | environmental magnetism | human dispersal

Anatomically modern human (AMH), or *Homo sapiens*, emerged in Africa at least 200 to 300 thousand years ago (ka) (1, 2). Integrated paleoclimatic and paleoanthropological data have shown that orbital-scale regional climate variability played a key role in driving AMH dispersal within Africa and to the adjacent Middle East (3–7). However, such integrated investigations remain sparse for South and East Asia, despite spanning a much larger areal extent and wider range of climatic and biographical zones than Africa, and hosting multiple important *H. sapiens* fossils dated back to ~100 ka (8–10) (Fig. 1). Moreover, South and East Asia serve as a land conduit through which AMH dispersed from Africa to Australia, Polynesia, and ultimately the Americas (8, 9) (Fig. 1). Thus, understanding *H. sapiens* fossils and archeological finds in appropriate paleoclimatic context is essential to developing a global perspective on AMH evolution and dispersal beyond Africa.

The Asian summer monsoon (ASM), comprising of the South (Indian) and East Asian submonsoon systems, governs moisture supply across low-latitude regions like the African monsoon, as well as to Asian latitudes as high as ~50°N, such as is observed in northeastern China (Fig. 1). This far-reaching areal extent, and hence, climatic impact of the ASM, is globally unique. After decades of proxy and modeling research, however, ASM dynamics and its orbital-scale variations remain a subject of scientific debate (12–23). Furthermore, the precise role of orbital ASM dynamics on early *H. sapiens* dispersal to East Asia is an important topic in both paleoclimatological and paleoanthropological research, yet our understanding of it remains limited due to the scarcity of integrated ASM and paleoanthropological studies.

Here, we develop insights into the climatic influence on the dispersal of AMH to East Asia and orbital-scale ASM dynamics over the last 280 thousand years (kyr). First, we study orbital-scale ASM dynamics by combining new centennial-resolution environmental magnetic records from the central Chinese Loess Plateau (CLP) with model-based continuous East Asian hydroclimate reconstructions (11) for the last 280 kyr. Second, we integrate proxy- and model-based spatiotemporal paleoclimatic reconstructions with Asian paleoanthropological and hydroclimatic data compilations and global *H. sapiens* habitat suitability simulations. We find that settling and dispersal conditions were optimal for the initial wave of AMH dispersal to East Asia during the last interglacial, when the stronger ASM caused warmer and more humid conditions, while the coeval Southeast African conditions became less favorable.

Significance

The precise role of climate shifts in early human dispersal to East Asia is important in paleoclimatology and paleoanthropology. Our proxy- and model-integrated paleoclimate reconstructions for the last 280 thousand years reveal a dynamic response of Asian summer monsoon variability to the combined effects of orbital-scale insolation, Northern Hemisphere ice volume, and greenhouse gas changes. By comparing paleoclimate data with a new compilation of *Homo sapiens* fossil and archaeological finds from Asia and simulated global *H. sapiens* habitat suitability, we show that orbitally modulated summer monsoon rainfall and temperature increases in East Asia concurrent with Southeast African climate deterioration may have promoted the early *H. sapiens* dispersal out of Africa, to the more remote region(s) of East Asia, during the last interglacial.

New ASM Records from the CLP

The CLP (~640,000 km^2) extends longitudinally from ~100 to 115°E and latitudinally from ~34 to 41°N (*SI Appendix*, Fig. S1). The present-day climate on the CLP is dominated by seasonally alternating southeasterly summer and northwesterly winter monsoon changes (23–25) (*SI Appendix*, Fig. S1). The southeasterly wind penetration inland from tropical oceans (Fig. 1) produces summer time (May to September) rain that accounts for ~60 to 75% of the annual total (23, 24). Materials forming CLP loess-paleosol deposits are transported predominantly by near-surface winter monsoon winds from upstream arid northwestern China (25–27). Within the loess package, the extent of soil formation depends on moisture availability that is governed by the ASM. Thus, the CLP loess-paleosol deposits can be used for paleomonsoon reconstructions (13, 23–26, 28).

Our study site, the Huanxian loess-paleosol section (107°15′E, 36°37′N), is located on the central CLP and sensitive to ASM penetration (*SI Appendix*, Fig. S1). In this section, the loess-paleosol sequence accumulated rapidly, with a sedimentation rate twice that of the classical sections located to the south and east. This enables investigation of the orbital-scale ASM variability at the Huanxian section in greater detail than typical. To measure ASM proxies in the laboratory, including magnetic susceptibility (χ) and anhysteretic remanent magnetization (ARM), we collected in the field 2,066 samples from the 44 m thick strata, which covers from Holocene paleosol S_0 to mid-Pleistocene loess L_3, ranging between marine isotope stage (MIS) 1 and MIS 8, at 2 to 2.5 cm intervals (equivalent to a temporal resolution of ~0.1 to 0.8 kyr). Our age model reconstruction for the Huanxian loess-paleosol section consists of two steps (cf. *Methods* and *SI Appendix*, Fig. S2). First, an initial age model was constructed through a detailed cycle-based correlation of χ with a globally averaged marine benthic foraminiferal $\delta^{18}O$ stack. Second, our final age model was based on a further, even more precise alignment, of our initial Huanxian loess-paleosol chronology to precisely U/Th-dated speleothem $\delta^{18}O$ records from East China (16). The support for our chronology construction comes independently from recent optically stimulated luminescence dating (29) (*SI Appendix*, Fig. S2D).

Rock magnetic analyses suggest that the Huanxian loess-paleosol magnetic properties are dominated by fine-grained magnetite/maghemite particles (*SI Appendix*, Figs. S3–S7 and Supplementary Text 1). Enhanced pedogenesis within the sediment column under wetter climate accelerates the formation of fine magnetite/maghemite particles, leading to higher χ and ARM values, and vice versa (24, 25). Therefore, the CLP loess-paleosol χ and ARM records are closely linked to the ASM precipitation. The lithological, χ, and ARM records from the Huanxian loess-paleosol section vary consistently over the last 280 kyr (Fig. 2 A–C). Paleosol layers (i.e., S_0, S_1, and S_2) have higher χ and ARM values than loess layers (i.e., L_1, L_2, and L_3), which is consistent with higher ASM precipitation during interglacials relative to glacials. The Huanxian χ and ARM records are marked by more square-wave ~100-kyr cycles, which differ slightly from the asymmetric glacial–interglacial structure in the global reference sea level/ice volume record (30) (Fig. 2 B–D). In addition to the ~100-kyr periodicity, Huanxian χ and ARM records are superimposed with lower-amplitude precessional (~20-kyr) variability, indicative of a possible low-latitude forcing linked to Northern Hemisphere summer insolation (NHSI). During MIS 5 and MIS 7, the superimposed precession-paced stadial substages occur close to NHSI minima and are not as dry as full glacial periods. During MIS 3–4 and early MIS 6, when glacial conditions were modest, somewhat moister interstadials occurred around NHSI maxima, albeit not

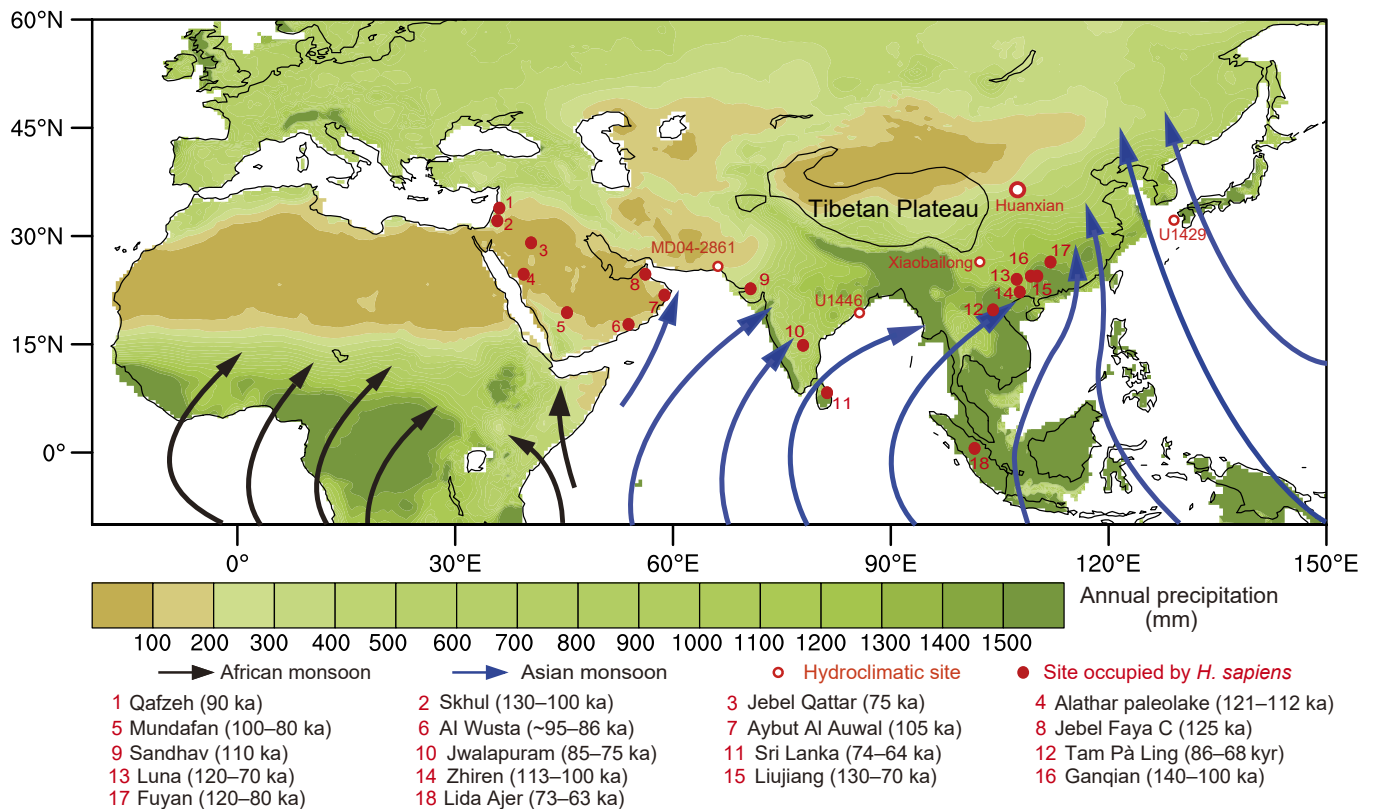**Fig. 1.** Study context. African and Eurasian annual precipitation map averaged between 130 and 70 ka from the latest model-based climate reconstructions (11), with referenced paleoclimatic and archeological sites in Asia, Tibetan Plateau (>2,000 m topography), and schematized African and Asian monsoon circulations. Background data for the listed Asian *H. sapiens* sites are included in *SI Appendix*, Table S1.
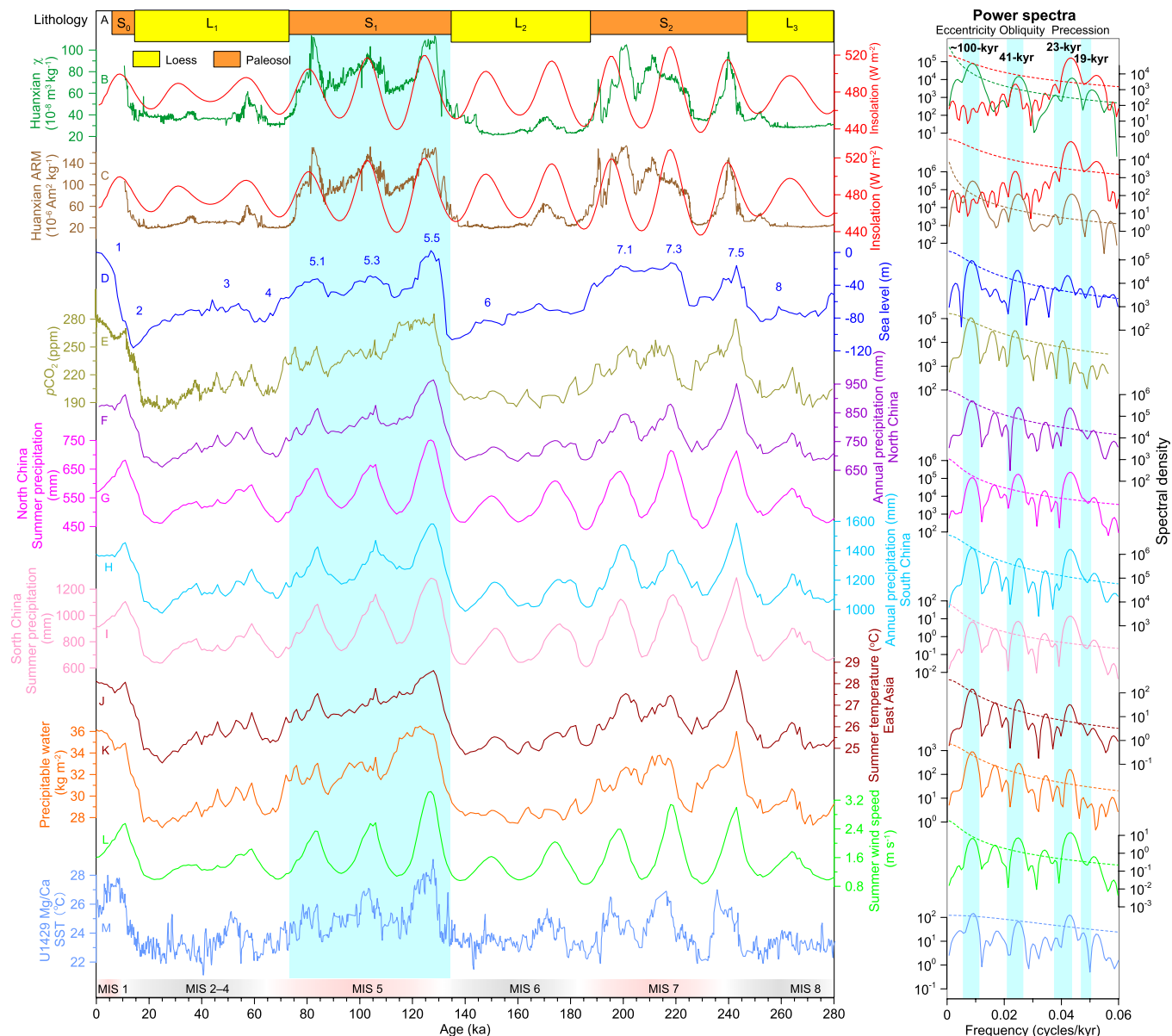
Fig. 2. Proxy- and model-based reconstructions of orbital-scale East Asian climate variability. (*A*) Lithology, (*B*) magnetic susceptibility (χ, green curve), and (*C*) ARM (brown curve) from the Huanxian loess-paleosol section with their comparison with 30°N July insolation (32) (red curve) and their power spectra. S-numbers and L-numbers refer to consecutive paleosol and loess horizons counting back from the present-day, respectively. Time series and power spectra of (*D*) sea level reconstruction from a global benthic foraminiferal $\delta^{18}O$ stack (30) and (*E*) atmospheric CO_2 reconstruction from Antarctic ice core (31). Numbers on the sea level record refer to the successive marine isotope stages. Time series and power spectra of (*F*) annual and (*G*) summer precipitation over North China (100–120°E; 30–45°N), (*H*) annual and (*I*) summer precipitation over South China (100–120°E; 20–30°N), (*J*) average summer surface temperature over low-latitude East Asia (100–120°E, 20°N), (*K*) summer precipitable moisture on the West Pacific and North Indian oceans (80–150°E; 0–35°N), (*L*) summer wind speed, in response to combined ice volume, atmospheric CO_2 concentration, and insolation forcing, which are calculated from the latest model-based climate reconstructions (11). Summer is represented by May to September. (*M*) International Ocean Discovery Program (IODP) Site U1429 Mg/Ca sea surface temperature (SST) record from the East China Sea (12) and its power spectrum. The dashed lines in the power spectra (*Right* panel) denote regions statistically significantly above the 95% confidence level (Student's *t* test). The vertical shading indicates the approximate timing of early AMH arrivals in East Asia.

as moist as interglacial periods (MIS 5 and MIS 7). However, during MIS 2–3, late MIS 6, and MIS 8, when glacial conditions were more extreme, aridity prevailed despite NHSI maxima. Spectral analyses of χ and ARM records confirm pervasive orbital cycles of eccentricity (~100-kyr), obliquity (41-kyr), and precession (~20-kyr), which are broadly comparable to the combined spectral results from NHSI, global average sea level, and atmospheric CO_2 records (30–32) (Fig. 2 *B–E*). The NHSI is characterized by a precessional cyclicity, whereas globally averaged sea level and atmospheric CO_2 records are dominated by a strong ~100-kyr eccentricity-paced cyclicity, with subdued expressions of obliquity- and precession-paced cycles.

Dynamics of Orbital-Scale ASM Variability

The cooccurring primary orbital cycles of ~100-kyr, 41-kyr, and ~20-kyr in the Huanxian loess-paleosol sequence cannot solely be explained by either an external (insolation) or internal (ice volume and greenhouse gas concentration) driver, but more likely through their combined action. Such an interpretation is further supported by a high-fidelity paleoclimate simulation, in which we utilized the climate output from a general circulation model forced by a combination of orbital-scale insolation, global ice volume, and atmospheric CO_2 forcing factors (model details are provided in ref. (11)). Model-based reconstructions of i) annual and summer (May to September) precipitation over North (100–120°E; 30–45°N) and

South China (100–120°E; 20–30°N), ii) low-latitude East Asian (100–120°E, 20°N) summer temperature, iii) summer precipitable moisture on the West Pacific and North Indian oceans (80–150°E; 0–35°N), and iv) summer wind speed show broadly similar orbital variability as our proxy records during the last 280 kyr, with combined eccentricity, obliquity, and precession cycles (Fig. 2). Therefore, both proxy- and model-based reconstructions support that the NHSI, ice volume, and greenhouse gas concentration jointly govern East Asian summer precipitation (13, 22, 23, 33).

In contrast to Huanxian records, the precession signal is largely subdued or absent in many χ records located to the south and east (*SI Appendix*, Figs. S1 and S8). However, like Huanxian records, precessional variability is prominent in the Jingyuan carbonate $\delta^{13}C$ record (23) and the Xijing spliced grain size-χ stack from the western CLP (21) and the Baoji ^{10}Be-based precipitation reconstruction from the southern CLP margin (13) (*SI Appendix*, Fig. S9). Thus, faint or absent precessional variability in those southern/eastern CLP loess-paleosol sections, which are usually associated with lower sedimentation rates, does not necessarily mean that CLP precipitation responded negligibly to precession-paced NHSI changes. Our Huanxian hydroclimatic records, together with the Jingyuan, Xijing, and Baoji hydroclimatic records (13, 21, 23), reveal a widespread presence of precessional ASM variability across the entire CLP, beyond the western sections or the southern CLP margin as recently recognized (13, 21, 23) (*SI Appendix*, Fig. S9). The distinct precession signal identified here, a typical monsoon pacing feature related to low-to-middle latitude insolation forcing (16, 17), together with our detailed rock magnetic results (*SI Appendix*, Figs. S3–S7 and Supplementary Text 1), supports the notion that the classical use of loess-paleosol χ as an ASM indicator (24, 25) is also (largely) valid for high sedimentation rate sections from the central CLP marked by higher ASM precipitation than the western CLP. However, secondary influences of pedogenic duration and temperature on χ cannot be fully excluded (21).

The precession signal in the Baoji ^{10}Be record is not as obvious as that seen in Huanxian, Jingyuan, and Xijing ASM records (*SI Appendix*, Fig. S9), which is possibly due to a lower sedimentation rate and data resolution as well as prominent gaps within MIS 5 and MIS 7. The Huanxian, Jingyuan, and Baoji records have a stronger ~100-kyr cyclicity than the Xijing record. These nuanced differences likely reflect variable responses of proxies to the extent of ASM precipitation. The Huanxian environmental magnetic records may be more directly related to regional ASM precipitation than the Jingyuan carbonate $\delta^{13}C$ record and Xijing spliced grain size-χ stack. Jingyuan carbonate $\delta^{13}C$ reflects local vegetation conditions likely linked to the complex interactions of precipitation, temperature, and CO_2 (21, 23). The Xijing spliced grain size-χ stack contains both ASM precipitation-induced χ variations and winter monsoon-related grain size changes (25–27).

To better document the ASM history across the entire CLP and minimize the limitations of specific proxy records, we compile a new ASM stack by summing the Huanxian χ and ARM records, the Jingyuan carbonate $\delta^{13}C$ record (23), the Xijing spliced grain size-χ stack (21), and the Baoji ^{10}Be record (13) (*SI Appendix*, Fig. S9). This new ASM stack shows consistency with East China composite speleothem $\delta^{18}O$ records (16) in portraying the precessional variability, although our ASM stack contains additionally ~100-kyr and 41-kyr cycles that are not distinct in the speleothem $\delta^{18}O$ records (Fig. 3 *A* and *B*). Nevertheless, cooccurring ~100-kyr, 41-kyr, and ~20-kyr periodicities have been captured by the Xiaobailong Cave $\delta^{18}O$ record from Southwest China (14), the $\delta^{18}O$ and δD_{wax} records from the Indian margin U1446 sediment core (18, 19), and the Arabian Sea summer monsoon stack (15) (Fig. 3). These records together provide an important Asian climatic context for AMH dispersal from Africa to East Asia.

Climatic Influence on Initial AMH Dispersal to East Asia

Multiple lines of fossil, archeological, and genetic evidence suggest that initial AMH arrivals in East Asia can be traced back to the last interglacial (more broadly MIS 5). Late Mid-Pleistocene to early Late Pleistocene sites with robust chrono-stratigraphic contexts and fossils that can be reasonably attributed to *H. sapiens* include South China localities such as Luna Cave (120 to 70 ka) (34), Zhiren Cave (113 to 100 ka) (35), and Fuyan Cave (120 to 80 ka) (36), that all range from ~130 ka to ~70 ka (Fig. 4*A*). Although a recent dating study on the Luna and Fuyan sites argued for younger ages (37), two follow-up studies criticized these younger ages by raising important flaws in its sampling procedures and species attributions, thereby suggesting that MIS 5 fossil ages remained feasible (38, 39); an interpretation we support. Similarly old hominin fossils tentatively attributed to *H. sapiens* were also reported from nearby Tongtianyan Cave (Liujiang, 130 to 70 ka) (40) and Ganqian Cave (140 to 100 ka) (41). Hominin fossils from Jimuyan (42), Dingcun (43), and Salawusu (43–45) have *H. sapiens* features, even though some primitive features in combination with larger age uncertainties make the interpretation of these fossils, in terms of AMH dispersal timing, relatively less unequivocal (43, 46). Likewise, two complete crania with closer affinities to *H. sapiens* but also some archaic features were reported from Ryonggok, North Korea (47, 48). Despite the fact that older ages were initially proposed for this finding, a younger age of 46 to 49 ka is currently more accepted (47, 48). Teeth from Lida Ajer Cave, Sumatra (73 to 63 ka) (49), suggest that AMH reached the island by ~70 ka. However, before settling in Sumatra, AMH must already have crossed mainland Southeast Asia (Fig. 1). Recently, this was confirmed by the *H. sapiens* presence at Tam Pà Ling (Northern Laos) between 86 ka and 68 ka (50) (Fig. 1). Moreover, the 65-ka-old sophisticated toolkit found in North Australia indicate that AMH possibly crossed Southeast Asian islands during late MIS 5 when regional climate remained favorable and relative sea level started to decline (8, 51). The AMH presence in Asia during MIS 5 is supported both by a large number of geochronologically dated fossils and artifacts (Figs. 1 and 4*A* and *SI Appendix*, Table S1) and by independent genetic studies (52, 53) that suggest the Asian presence of modern human lineages earlier than 75 ka. Lastly, it is additionally supported by a recent finding that a deeply divergent modern humans contributed genetically to the ancestry of Altai Neanderthals by roughly 100 ka (53). We are cognizant of the inherent dating uncertainties associated with a few hominin sites and the debate regarding their species attribution (54, 55), so we do not attempt to distinguish AMH dispersal time to either the earlier or later part of MIS 5. Nevertheless, the available data confirm initial AMH arrivals in East Asia by the last interglacial (8).

The AMH occupation in MIS 5 East Asia (Fig. 4*A*) coincided with regional rain and temperature increases as seen in our proxy- and model-based reconstructions and existing paleoclimatic records from Asia (Figs. 2 and 3). To further examine ASM climate influence on AMH dispersal, we analyze *H. sapiens* habitats from a recently established transient Pleistocene simulation of this kind (7). This multidimensional statistical model simulates the habitat suitability for *H. sapiens* occupation at a given location and time, by quantifying the relationships among geochronologically dated fossil/archeological data and different climatic variables of biological importance, i.e., yearly precipitation minimum, annual mean precipitation, temperature, and net primary productivity (7). The simulated *H. sapiens* habitat suitability over East Asia (80–130°E; 20–55°N) shows large temporal variation during the last 280 kyr (Fig. 4*B*), with both ~100-kyr and ~20-kyr cyclicities comparable to the aforementioned Asian hydroclimatic oscillations (Figs. 2 and 3). Interestingly, the temporal increases in simulated East Asian *H. sapiens* habitat
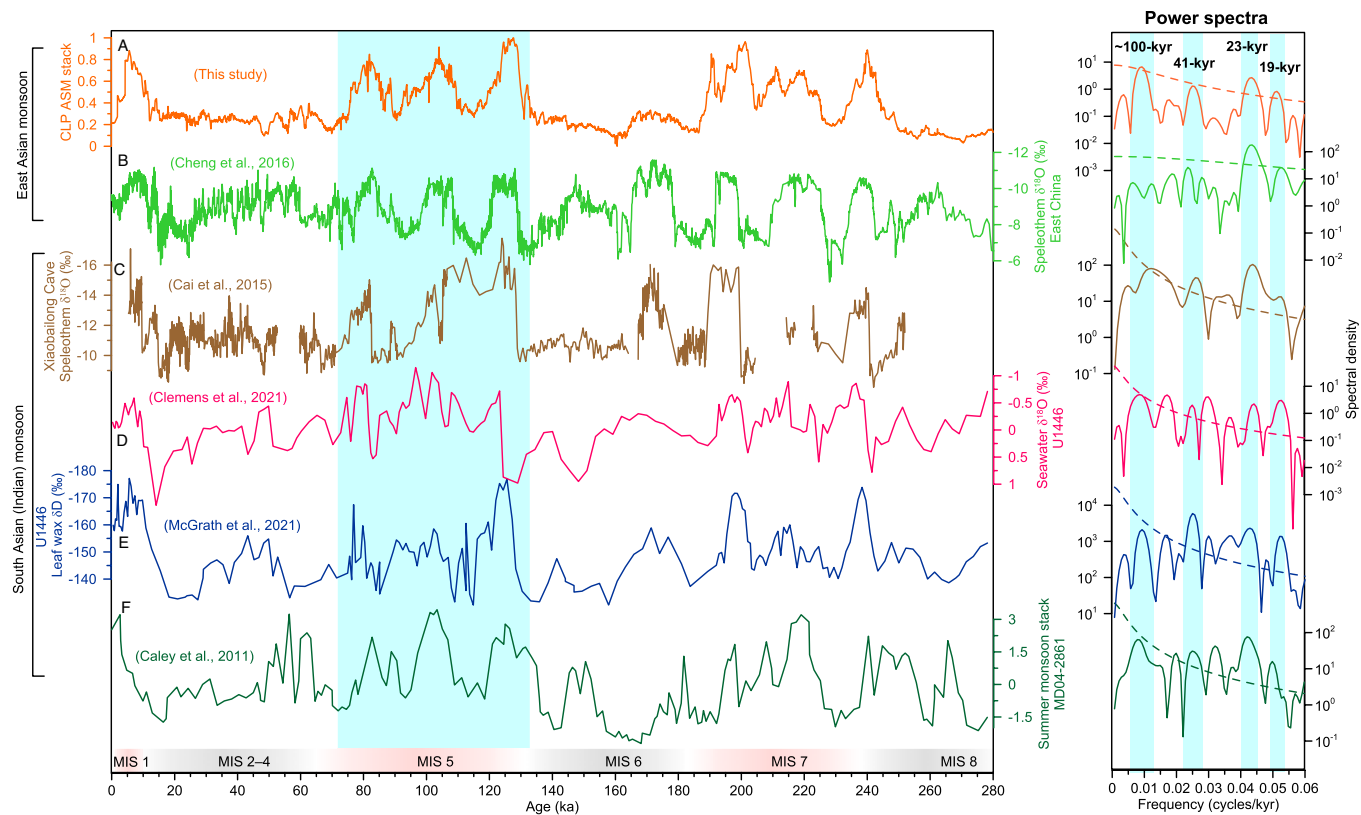
Fig. 3. Climatic context for early *H. sapiens* dispersal to East Asia. Time series and power spectra of (*A*) new CLP ASM stack based on the Huanxian χ and ARM records, the Jingyuan carbonate δ¹³C record (23), the Xijing spliced grain size-χ stack (21), and the Baoji ¹⁰Be-based precipitation record (13), (*B*) China composite speleothem δ¹⁸O record (16), (*C*) speleothem δ¹⁸O from Xiaobailong Cave, South China (14), (*D* and *E*) Indian margin Site U1446 sediment core seawater δ¹⁸O and δD_wax records (18, 19), and (*F*) summer monsoon stack from sediment core MD04-2861, Arabian Sea (15). The vertical shading indicates the approximate timing of early AMH arrivals in East Asia.

peaked at ~120, ~95, and ~70 ka, in comparison to the preceding glacial MIS 6 (Fig. 4*B*). This is coeval with the orbitally modulated ASM strengthening (Figs. 2 and 3) and the earliest AMH fossil occurrences in East Asia (Fig. 4*A* and *SI Appendix*, Table S1). We argue that the ASM strengthening in MIS 5 induced i) regional precipitation increases (Figs. 2 and 3), ii) a greener, more lushly vegetated East Asia, and iii) more abundant food resources, which would have benefited expansion in the ranges of various fauna, including *H. sapiens* (56). Such optimum environmental conditions, together with the greater climatic tolerance of *H. sapiens* that developed during ~300 to 100 ka (4, 7), plausibly provided an unprecedented opportunity for AMH dispersal to East Asia during the last interglacial. According to the habitat map averaged over 125 to 70 ka (Fig. 4*C*), transcontinental optimal habitats might have stimulated AMH populations to disperse from their African homeland to East Asia via southern (South Asia) and northern routes (continental Central Asia). An earlier (pre-70-ka) AMH dispersal utilizing the southern route to East Asia is most consistent with ASM strengthening (Fig. 3). Moreover, the southern dispersal route lies under strong, continual ASM influence and is supported by the MIS 5 AMH archeological evidence from India, including the sites of Sandhav (~110 ka) (57), Katoati (96 ka) (58), Jwalapuram (85 to 75 ka) (59), and Sri Lanka (74 to 64 ka) (58) (Figs. 1 and 4*C*). Although recent findings suggest that early *H. sapiens* may have dispersed to Greece (Europe) and Israel (West Asia) as early as ~200 ka (60, 61), *H. sapiens* fossil/archeological evidence remains currently absent from MIS 6–5 Central Asia (8). This absence probably indicates that the relatively colder/drier northern dispersal route beyond the ASM reach may have occurred later than the southern route (8, 62), possibly with an initial failure in competition with preexisting populations of Denisovans or Neanderthals (36, 63) (Fig. 4*C*).

Before the *H. sapiens* appearance, East Asia was occupied by a number of hominins characterized by a mosaic of plesiomorphic features with derived traits (such as enlarged cranial capacity, facial gracilization, simplified enamel-dentine junction surfaces, or symmetrical premolar crowns). These samples include fossils recovered from either Huanglong Cave, Harbin, Panxian Dadong, Xuchang, Dali, or Tongzi (43, 64–70). They have been tentatively classified as "non-erectus" Asian Mid-Pleistocene hominins (65, 70). However, we find that the large majority of East Asian *H. sapiens* and other hominin sites older than 70 ka are consistently under ASM influence. Lower latitudes with higher ASM precipitation contain more hominin sites of the late Mid-Pleistocene and early Late Pleistocene than higher latitudes with lower ASM precipitation. Particularly, almost all robustly dated pre-70-ka *H. sapiens* evidence is found from Southeast Asia with wetter and greener landscapes under continual ASM influence. These observations are consistent with a close link between hominin occupation and the ASM. The ASM-induced changes in the habitats of East Asian hominins affected their mobility and possibly their degrees of isolation, which in turn may have affected the probability of their mixing and interbreeding (71). Although we are far from understanding the phenotypic signal of interbreeding (72), we cannot rule out that part of the anatomical variability of the late-Middle to Late Pleistocene groups in Asia is related to the admixture of *H. sapiens* with the pre-existing indigenous populations at the time of AMH's arrival (73).

In contrast to a shift to wetter conditions in East Asia induced by ASM strengthening as suggested by both our proxy- and model-based hydroclimatic reconstructions (Fig. 2), large areas of Southeast Africa—the major homeland of *H. sapiens*—had a deteriorating climate during the MIS 6–5 transition (3, 74–78). For example, paleoclimatic records from the Limpopo catchment, KwaZulu-Natal, and Lake Magadi
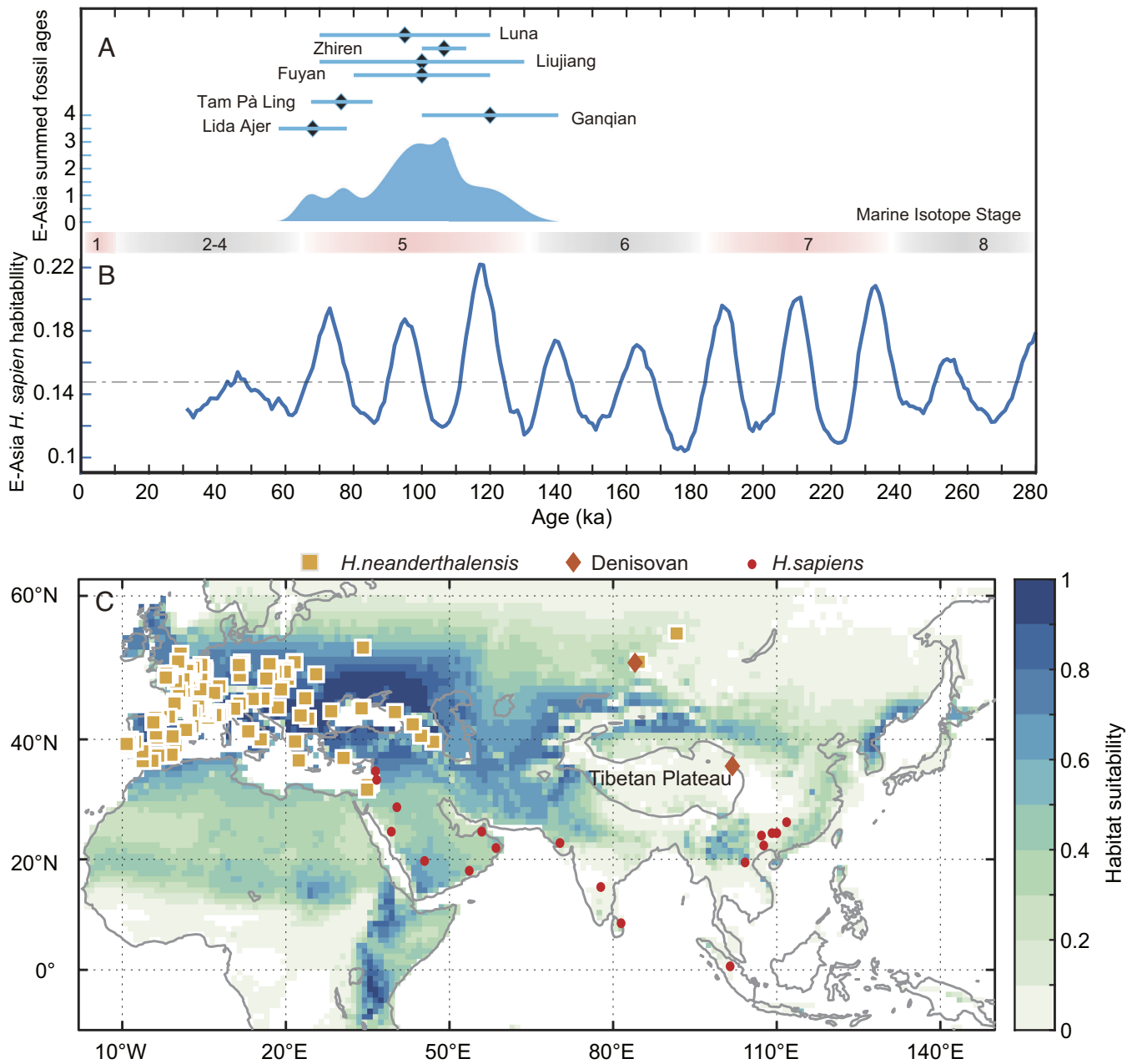
Fig. 4. *Homo sapiens* habitat suitability. (*A*) Raw and aggregated age distributions of early *H. sapiens* fossils from China, including Luna Cave (120 to 70 ka) (34), Zhiren Cave (113 to 100 ka) (35), Tongtianyan Cave (Liujiang, 130 to 70 ka) (40), Ganqian Cave (140 to 100 ka) (41), and Fuyan Cave (120 to 80 ka) (36), and from Southeast Asia represented by Tam Pà Ling (86 to 68 ka) in Northern Laos (50) and Lida Ajer Cave (73 to 63 ka) in Sumatra (49). (*B*) Simulated timeseries of *H. sapiens* habitat suitability in East Asia during the last 280 kyr and (*C*) simulated *H. sapiens* habitat map over 125 to 70 ka (7) with occupied localities by *H. neanderthalensis*, possible Denisovans, and early *H. sapiens*.

suggest a series of "megadroughts" in subtropical Southeast Africa during MIS 5 (74–76). A principal component analysis of hydrologically sensitive fossil and mineralogical records from Lake Malawi suggests that tropical Southeast Africa was largely drier during MIS 5 relative to MIS 6 (78). The deterioration of climatic conditions could have decreased vegetation and reduced mammal populations and the availability of resources and habitats. This is confirmed by our *H. sapiens* habitat simulation, which suggests that habitat peaks and troughs in East Africa and habitat peaks in South Africa lowered during MIS 5, in comparison to the preceding MIS 6 (*SI Appendix*, Fig. S10). This in turn enhanced selective pressures, so *H. sapiens* may have been forced to expand beyond Africa and into the nearby West Asia. Upon arrival of *H. sapiens* populations in the West Asian regions around the Mediterranean Sea, as indicated by evidence from Israel (79–81), some may have dispersed further to remote East Asia during

MIS 5, when increased ASM precipitation produced suitable conditions with abundant resources (e.g., food, water, and shelter), attracting *H. sapiens* colonization. The combination of concurrent climate deterioration in large areas of Southeast African and favorable climate in East Asia may have promoted continental-scale early *H. sapiens* dispersal to East Asia during MIS 5.

To summarize, through synthesis of new proxy- and model-based East Asian climate reconstructions, compilations of Asian paleoanthropological and paleoclimatic data, and *H. sapiens* habitat simulations through time and space, we improve current understanding of orbital-scale ASM dynamics, and more importantly, reveal the close links between ASM climate and initial AMH dispersal to East Asia. New centennial-resolution environmental magnetic records derived from a unique high sedimentation rate loess-paleosol section on the central CLP, together with the latest proxy records from

other parts of the plateau (13, 21, 23), document a pervasive precession signal in the hydroclimatic evolution across the CLP, in addition to the well-recognized ~100-kyr cyclicity. Our results provide new evidence from Asia for previously suggested complex models explaining the origin and dispersal(s) of *H. sapiens*, which points to less linear evolutionary scenarios where climatic changes likely played a major role in the dispersals, fragmentation, assimilation, and recombination of new immigrant populations with preexisting local groups (71, 82, 83). Integration of paleoclimate data with compiled hominin fossil and archeological finds from Asia and simulated *H. sapiens* habitats shows that increased monsoonal rain and higher temperature across the Asian continent, together with climate deterioration in Southeast Africa, provided an optimum window of opportunity for early AMH dispersals to remote East Asia during the last interglacial.

Methods

Following removal of weathered surface outcrop, 2,066 fresh samples were collected from paleosol S_0 (MIS 1) to loess L_3 (MIS 8) at 2 to 2.5 cm intervals (equivalent to ~0.1 to 0.8 kyr time spacing) from the Huanxian loess-paleosol section. About 10 g of each sample was powdered and then packed into a nonmagnetic cubic box (2 × 2 × 2 cm) for χ and ARM measurements in the laboratory. We measured room temperature χ using a SM-150L magnetic susceptibility meter (ZH instruments, Czech Republic) at a frequency of 500 Hz and an applied field of 80 A/m at the Institute of Earth Environment, Chinese Academy of Sciences, Xi'an, China. ARM was imparted using a peak alternating field (AF) of 100 mT and a 0.05 mT direct current (DC) bias field and was measured using a 2-G Enterprises Model 755 cryogenic magnetometer housed in a magnetically shielded space at the China University of Geosciences (Wuhan), China.

We established a first-order chronology for the Huxian loess-paleosol section based on the well-identified cycle-based correlation between CLP loess-paleosol χ and marine benthic foraminiferal $\delta^{18}O$ records (24, 25) (*SI Appendix*, Fig. S2 A and B). In addition to the top and bottom points, six extra points around the transitions between high and low χ units were used as tie points to construct this first-order chronology (*SI Appendix*, Fig. S2B). Both CLP χ and East China speleothem $\delta^{18}O$ records are grossly linked to the same large-scale shifts in ASM circulation (16, 24, 25, 84). We further refined the first-order chronology by repeatedly matching χ with the precisely dated composite East China speleothem $\delta^{18}O$ record (16) in an objective way until their cycles are synchronized to in-phase variations (*SI Appendix*, Fig. S2C). This recently developed approach enables a more precise speleothem-based CLP loess-paleosol chronology relative to previous age models based on land-sea correlation or orbital tuning (13, 28, 85). In addition to the eight points selected for the first-order chronology construction, we selected seven additional tie points either located on high-amplitude χ peaks of the well-developed strong pedogenic interglacial paleosol S_2 or at the onset/termination of relatively weaker pedogenic subpaleosols (corresponding to somewhat moister interstadials and lower-amplitude χ peaks) within glacial loess layers, to construct the refined age model for the Huanxian loess-paleosol section based on cyclic correlation between the χ and East China speleothem $\delta^{18}O$ records (*SI Appendix*, Fig. S2C). This refined chronology is supported independently by recent optically stimulated luminescence dating of the Jingbian loess-paleosol section on the northern CLP margin (29) (*SI Appendix*, Fig. S2D). The Huanxian χ data on the refined chronology closely follow the speleothem $\delta^{18}O$ record over precessional cycles (*SI Appendix*, Fig. S2C). Land–sea correlation and loess-speleothem match, with distinct tie point selection, do not result in significant differences in the CLP loess-paleosol age models, generally with only millennial differences (23–26, 28).

We established a new ASM stack by compiling proxy records from East Asia, including the Huanxian χ and ARM records, the Jingyuan carbonate $\delta^{13}C$ record (23), the Xijing spliced grain size-χ stack (21), and the Baoji ^{10}Be-based precipitation reconstruction (13). Like our established Huanxian χ and ARM time series above, we first refined age models for the Jingyuan carbonate $\delta^{13}C$ record (23), Xijing spliced grain size-χ stack (21), and Baoji ^{10}Be-based precipitation record (13) by synchronizing them to the precisely U/Th-dated East China speleothem $\delta^{18}O$ record (16). After synchronization, we used the interpolating function in the *Acycle* software (86) to conservatively resample all used records at 0.5-kyr intervals to obtain evenly spaced data series. We constructed the ASM stack from

the CLP by averaging the evenly spaced Huanxian χ and ARM, Jingyuan carbonate $\delta^{13}C$, Xijing spliced grain size-χ stack, and Baoji ^{10}Be-based precipitation time series with equal weight. To evaluate the robustness of the orbital signature, we used the smoothed periodogram to analyze the power spectra of proxy- and model-based paleoclimatic reconstructions with the function Spectral Analysis in the *Acycle* software (86), with a bandwidth of 2 and a sampling interval of 1 kyr.

To identify the magnetic minerals in the sediments, we measured temperature-dependent magnetic susceptibility curves (χ–T), isothermal remanent magnetization (IRM) acquisition curves, magnetic hysteresis loops, first-order reversal curve (FORC) diagrams, and low-temperature cycles of the saturation isothermal remanent magnetization (SIRM) for nine samples from the Huanxian section at the Institute of Earth Environment, Chinese Academy of Sciences, Xi'an, China. They contain four loess samples from loess layers L_1, L_2, and L_3 and five paleosol samples from paleosol layers S_0, S_1, and S_2. χ–T curves were measured in an argon atmosphere from room temperature to 700 °C and back to room temperature with a MFK1-FA susceptometer equipped with a CS-3 high-temperature furnace (AGICO, Brno, Czech Republic). IRM acquisition curves, magnetic hysteresis loops, and FORC diagrams were measured with a Princeton Measurements Corporation (Model 3900) vibrating sample magnetometer (VSM). Each IRM acquisition curve contains 200 data points measured at logarithmically spaced field steps to 1 T. Each hysteresis loop was measured between ±1 T at 3 mT increments, with a 300 ms averaging time. For each sample, 80 FORCs were measured at 5 mT increments to ~600 mT, with a 100 ms averaging time. Low-temperature magnetic measurements were conducted with a Quantum Design superconducting quantum interference device (SQUID) Magnetic Property Measurement System (MPMS) (Quantum Design Inc.). A room temperature saturation isothermal remanent magnetization (SIRM), which was imparted in a 5 T field at 300 K, was measured at 5 K intervals from 300 to 5 K and back to 300 K in zero magnetic field.

Data, Materials, and Software Availability. Measured proxy data have been deposited in East Asian Paleoenvironmental Science Database (https://dx.doi.org/10.12262/IEECAS.EAPSD2023012) (87). All other data are included in the manuscript and/or supporting information.

Author affiliations: [a]State Key Laboratory of Loess and Quaternary Geology, Institute of Earth Environment, Chinese Academy of Sciences, Xi'an 710061, China; [b]Laoshan Laboratory, Qingdao 266237, China; [c]Center for Climate Physics, Institute for Basic Science, Busan 46241, South Korea; [d]Pusan National University, Busan 46241, South Korea; [e]Dental Anthropology Group, National Research Center on Human Evolution, Burgos 09002, Spain; [f]Department of Anthropology, University College London, London WC1H 0BW, United Kingdom; [g]Department of Zoology, University of Cambridge, Cambridge CB2 1TN, United Kingdom; [h]Department of Earth and Environmental Sciences, The University of Manchester, Manchester M13 9PL, United Kingdom; [i]Palaeomagnetic Laboratory 'Fort Hoofddijk', Department of Earth Sciences, Faculty of Geosciences, Utrecht University, Utrecht 3584 CD, The Netherlands; [j]Bordeaux Institut National Polytechnique, Environnements et Paléoenvironnements Océaniques et Continentaux, University of Bordeaux, Centre national de la recherche scientifique, UMR 5805, Pessac F-33600, France; [k]School of Geographical and Earth Sciences, University of Glasgow, Glasgow G12 8QQ, United Kingdom; [l]School of Earth Sciences, China University of Geosciences, Wuhan 430074, China; [m]College of Geology and Environment, University of Science and Technology, Xi'an 710054, China; [n]College of Life Science, Shanxi Normal University, Taiyuan 030031, China; [o]Institute of Global Environmental Change, Xi'an Jiaotong University, Xi'an 710049, China; and [p]Interdisciplinary Research Center of Earth Science Frontier, Beijing Normal University, Beijing 100875, China

Author contributions: H.A. and Z.A. designed research; H.A., J.R., M.K., C.H., Xinxia Li, Z. Zhang, J.J., and X.X. performed research; H.A., J.R., M.K., and Z. Zhu contributed new reagents/analytic tools; H.A., J.R., M.K., D.L., M.J.D., Xinxia Li, Q.S., P.Y., Xinzhou Li, Y.S., X.Q., P.Z., and Z.A. analyzed data; C.H. contributed to helpful discussions; and H.A., J.R., M.M.-T., D.L., M.J.D., T.C., and T.N.J. wrote the paper.

1. J. J. Hublin *et al.*, New fossils from Jebel Irhoud, Morocco and the pan-African origin of *Homo sapiens*. *Nature* **546**, 289–292 (2017).
2. C. M. Vidal *et al.*, Age of the oldest known *Homo sapiens* from eastern Africa. *Nature* **601**, 579–583 (2022).
3. J. E. Tierney, P. B. deMenocal, P. D. Zander, A climatic context for the out-of-Africa migration. *Geology* **45**, 1023–1026 (2017).
4. R. M. Beyer, M. Krapp, A. Eriksson, A. Manica, Climatic windows for human migration out of Africa in the past 300,000 years. *Nat. Commun.* **12**, 4889 (2021), 10.1038/s41467-021-24779-1.
5. F. Schaebitz *et al.*, Hydroclimate changes in eastern Africa over the past 200,000 years may have influenced early human dispersal. *Commun. Earth Environ.* **2**, 123 (2021), 10.1038/s43247-021-00195-7.
6. A. Timmermann, T. Friedrich, Late Pleistocene climate drivers of early human migration. *Nature* **538**, 92–95 (2016).
7. A. Timmermann *et al.*, Climate effects on archaic human habitats and species successions. *Nature* **604**, 495–501 (2022).
8. C. J. Bae, K. Douka, M. D. Petraglia, On the origin of modern humans: Asian perspectives. *Science* **358**, eaai9067 (2017).
9. R. Dennell, *From Arabia to the Pacific: How Our Species Colonised Asia* (Routledge, London, UK, 2020), p. 386.
10. C. J. Bae, F. Li, L. L. Cheng, W. Wang, H. L. Hong, Hominin distribution and density patterns in Pleistocene China: Climatic influences. *Palaeogeogr. Palaeoclimatol. Palaeoecol.* **512**, 118–131 (2018).
11. M. Krapp, R. M. Beyer, S. L. Edmundson, P. J. Valdes, A. Manica, A statistics-based reconstruction of high-resolution global terrestrial climate for the last 800,000 years. *Sci. Data* **8**, 228 (2021), 10.1038/s41597-021-01009-3.
12. S. C. Clemens *et al.*, Precession-band variance missing from East Asian monsoon runoff. *Nat. Commun.* **9**, 3364 (2018), 10.1038/s41467-018-05814-0.
13. J. W. Beck *et al.*, A 550,000-year record of East Asian monsoon rainfall from ^{10}Be in loess. *Science* **360**, 877–881 (2018).
14. Y. J. Cai *et al.*, Variability of stalagmite-inferred Indian monsoon precipitation over the past 252,000 y. *Proc. Natl. Acad. Sci. U.S.A.* **112**, 2954–2959 (2015).
15. T. Caley *et al.*, New Arabian Sea records help decipher orbital timing of Indo-Asian monsoon. *Earth Planet. Sci. Lett.* **308**, 433–444 (2011).
16. H. Cheng *et al.*, The Asian monsoon over the past 640,000 years and ice age terminations. *Nature* **534**, 640–646 (2016).
17. H. Cheng *et al.*, Milankovitch theory and monsoon. *Innovation* **3**, 100338 (2022), 10.1016/j.xinn.2022.100338.
18. S. C. Clemens *et al.*, Remote and local drivers of Pleistocene South Asian summer monsoon precipitation: A test for future predictions. *Sci. Adv.* **7**, eabg3848 (2021).
19. S. M. McGrath, S. C. Clemens, Y. S. Huang, M. Yamamoto, Greenhouse gas and ice volume drive Pleistocene Indian summer monsoon precipitation isotope variability. *Geophys. Res. Lett.* **48**, e2020GL092249, (2021), 10.1029/2020GL092249.
20. D. Gebregiorgis *et al.*, Southern Hemisphere forcing of South Asian monsoon precipitation over the past ~1 million years. *Nat. Commun.* **9**, 4702 (2018), 10.1038/s41467-018-07076-2.
21. B. H. Guo *et al.*, Dominant precessional forcing of the East Asian summer monsoon since 260 ka. *Geology* **50**, 1372–1376 (2022).
22. Y. B. Sun *et al.*, Astronomical and glacial forcing of East Asian summer monsoon variability. *Quat. Sci. Rev.* **115**, 132–142 (2015).
23. Y. B. Sun *et al.*, Diverse manifestations of the mid-Pleistocene climate transition. *Nat. Commun.* **10**, 352 (2019), 10.1038/s41467-41018-08257-41469.
24. H. Ao *et al.*, Two-stage mid-Pleistocene climate transition and mid-Pleistocene human diversification. *Earth-Sci. Rev.* **210**, 103354 (2020).
25. Q. Z. Hao *et al.*, Delayed build-up of Arctic ice sheets during 400,000-year minima in insolation variability. *Nature* **490**, 393–396 (2012).
26. Z. L. Ding *et al.*, Stacked 2.6-Ma grain size record from the Chinese loess based on five sections and correlation with the deep-sea δ^{18}O record. *Paleoceanography* **17**, 1033 (2002).
27. Y. B. Sun, S. C. Clemens, Z. S. An, Z. W. Yu, Astronomical timescale and palaeoclimatic implication of stacked 3.6-Myr monsoon records from the Chinese Loess Plateau. *Quat. Sci. Rev.* **25**, 33–48 (2006).
28. Y. B. Sun *et al.*, High-sedimentation-rate loess records: A new window into understanding orbital- and millennial-scale monsoon variability. *Earth-Sci. Rev.* **220**, 103731 (2021).
29. T. Stevens *et al.*, Ice-volume-forced erosion of the Chinese Loess plateau global quaternary stratotype site. *Nat. Commun.* **9**, 983 (2018).
30. E. J. Rohling *et al.*, Sea level and deep-sea temperature reconstructions suggest quasi-stable states and critical transitions over the past 40 million years. *Sci. Adv.* **7**, eabf5326 (2021).
31. B. Bereiter *et al.*, Revision of the EPICA Dome C CO_2 record from 800 to 600 kyr before present. *Geophys. Res. Lett.* **42**, 542–549 (2015).
32. J. Laskar, A. Fienga, M. Gastineau, H. Manche, La2010: A new orbital solution for the long term motion of the Earth. *Astron. Astrophys.* **532**, A89 (2011).
33. Z. K. Zhang, G. J. Li, Y. J. Cai, Z. Y. Liu, Z. S. An, Variation of summer precipitation δ^{18}O on the Chinese Loess Plateau since the last interglacial. *J. Quat. Sci.* **36**, 1214–1220 (2021).
34. C. J. Bae *et al.*, Modern human teeth from Late Pleistocene Luna Cave (Guangxi, China). *Quat. Int.* **354**, 169–183 (2014).
35. W. Liu *et al.*, Human remains from Zhirendong, South China, and modern human emergence in East Asia. *Proc. Natl. Acad. Sci. U.S.A.* **107**, 19201–19206 (2010).
36. W. Liu *et al.*, The earliest unequivocally modern humans in southern China. *Nature* **526**, 696–699 (2015).
37. X. F. Sun *et al.*, Ancient DNA and multimethod dating confirm the late arrival of anatomically modern humans in southern China. *Proc. Natl. Acad. Sci. U.S.A.* **118**, e2019158118 (2021).
38. M. Martinón-Torres *et al.*, On the misidentification and unreliable context of the new "human teeth" from Fuyan Cave (China). *Proc. Natl. Acad. Sci. U.S.A.* **118**, e2102961118 (2021).
39. T. F. G. Higham, K. Douka, The reliability of late radiocarbon dates from the Paleolithic of southern China. *Proc. Natl. Acad. Sci. U.S.A.* **118**, e2103798118 (2021).
40. G. J. Shen *et al.*, U-Series dating of Liujiang hominid site in Guangxi, Southern China. *J. Hum. Evol.* **43**, 817–829 (2002).
41. G. J. Shen, W. Wang, Q. Wang, Y. J. Pan, U-series dating of hominid site Ganqian Cave at Tubo, Liujiang, Guangxi in South China. *Acta Anthropol. Sin.* **20**, 238–244 (2001).
42. W. Wang, C. L. Huang, S. W. Xie, C. L. Yan, Late Pleistocene hominin teeth from the Jimuyan Cave, Pingle County, Guangxi, South China. **31**, 699–704 (2011).
43. W. Liu, X. J. Wu, S. Xing, Y. Y. Zhang, *Human Fossils in China* (Science Press, Beijing, China, 2014), p. 388.
44. H. Shang, W. Liu, X. Z. Wu, G. R. Dong, Upper Pleistocene human scapula from Salawusu, Inner Mongolia, China. *Chin. Sci. Bull.* **51**, 2110–2115 (2006).
45. H. Shang, Q. Wei, X. H. Wu, An issue on the date of fossil human remains from Sala Wusu, Inner Mongolia. *Acta Anthropol. Sin.* **25**, 82–86 (2006).
46. M. Martinón-Torres, X. J. Wu, J. M. Bermúdez de Castro, S. Xing, W. Liu, *Homo sapiens* in the Eastern Asian Late Pleistocene. *Curr. Anthropol.* **58**, S434–S448 (2017).
47. C. Bae, P. Guyomarc'h, Potential contributions of Korean Pleistocene hominin fossils to palaeoanthropology: A view from Ryonggok Cave. *Asian Perspect.* **54**, 31–57 (2015).
48. C. J. Norton, The current state of Korean paleoanthropology. *J. Hum. Evol.* **38**, 803–825 (2000).
49. K. E. Westaway *et al.*, An early modern human presence in Sumatra 73000–63000 years ago. *Nature* **548**, 322–325 (2017).
50. S. E. Freidline *et al.*, Early presence of *Homo sapiens* in southeast Asia by 86–68 kyr at Tam Pà Ling, Northern Laos. *Nat. Commun.* **14**, 3193 (2023), 10.1038/s41467-023-38715-y.
51. C. Clarkson *et al.*, Human occupation of northern Australia by 65,000 years ago. *Nature* **547**, 306–310 (2017).
52. L. Pagani *et al.*, Genomic analyses inform on migration events during the peopling of Eurasia. *Nature* **538**, 238–242 (2016).
53. M. Kuhlwilm *et al.*, Ancient gene flow from early modern humans into Eastern Neanderthals. *Nature* **530**, 429–433 (2016).
54. R. Dennell, Early *Homo sapiens* in China. *Nature* **468**, 512–513 (2010).
55. R. Dennell, M. D. Petraglia, The dispersal of *Homo sapiens* across southern Asia: How early, how often, how complex? *Quat. Sci. Rev.* **47**, 15–22 (2012).
56. I. A. Lazagabaster *et al.*, Rare crested rat subfossils unveil Afro-Eurasian ecological corridors synchronous with early human dispersals. *Proc. Natl. Acad. Sci. U.S.A.* **118**, e2105719118 (2021).
57. J. Blinkhorn *et al.*, The first directly dated evidence for Palaeolithic occupation on the Indian coast at Sandhav, Kachch. *Quat. Sci. Rev.* **224**, 105975 (2019), 10.1016/j.quascirev.2019.105975.
58. J. Blinkhorn, M. D. Petraglia, Environments and cultural change in the Indian subcontinent: Implications for the dispersal of *Homo sapiens* in the Late Pleistocene. *Curr. Anthropol.* **58**, 463–479 (2017).
59. M. Petraglia *et al.*, Middle Paleolithic assemblages from the Indian subcontinent before and after the Toba super-eruption. *Science* **317**, 114–116 (2007).
60. K. Harvati *et al.*, Apidima Cave fossils provide earliest evidence of *Homo sapiens* in Eurasia. *Nature* **571**, 500–504 (2019).
61. I. Hershkovitz *et al.*, The earliest modern humans outside Africa. *Science* **359**, 456–459 (2018).
62. T. Goebel, "The overland dispersal of modern humans to eastern Asia: An alternative, northern route from Africa" in *Emergence and Diversity of Modern Human Behavior in Paleolithic*, Y. Kaifu, T. Goebel, H. Sato, A. Ono, Eds. (Texas A&M University Press, College Station, TX, 2015), pp. 437–452.
63. N. Zwyns *et al.*, The northern route for human dispersal in central and northeast Asia: New evidence from the site of Tolbor-16, Mongolia. *Sci. Rep.* **9**, 1–10 (2019).
64. X. J. Ni *et al.*, Massive cranium from Harbin in northeastern China establishes a new Middle Pleistocene human lineage. *Innovation* **2**, 100130 (2021), 10.1016/j.xinn.2021.100130.
65. S. Xing, M. Martinón-Torres, J. M. Bermúdez de Castro, Late Middle Pleistocene hominin teeth from Tongzi, Southern China. *J. Hum. Evol.* **130**, 96–108 (2019).
66. W. Liu *et al.*, Late Middle Pleistocene hominin teeth from Panxian Dadong, South China. *J. Hum. Evol.* **64**, 337–355 (2013).
67. Z. Y. Li *et al.*, Late Pleistocene archaic human crania from Xuchang, China. *Science* **355**, 969–972 (2017).
68. X. Z. Wu, S. Athreya, A description of the geological context, discrete traits, and linear morphometrics of the Middle Pleistocene hominin from Dali, Shaanxi Province, China. *Am. J. Phys. Anthropol.* **150**, 141–157 (2013).
69. X. J. Wu *et al.*, Archaic human remains from Hualongdong, China, and Middle Pleistocene human continuity and variation. *Proc. Natl. Acad. Sci. U.S.A.* **116**, 9820–9824 (2019).
70. X. J. Wu *et al.*, Morphological and morphometric analyses of a late Middle Pleistocene hominin mandible from Hualongdong, China. *J. Hum. Evol.* **182**, 103411 (2023), 10.1016/j.jhevol.2023.103411.
71. R. Dennell, M. Martinón-Torres, J.-M. Bermúdez de Castro, G. Xing, A demographic history of Late Pleistocene China. *Quat. Int.* **559**, 4–13 (2020).
72. R. R. Ackermann, Phenotypic traits of primate hybrids: Recognizing admixture in the fossil record. *Evol. Anthropol.* **19**, 258–270 (2010).
73. W. Liao *et al.*, Mosaic dental morphology in a terminal Pleistocene hominin from Dushan Cave in southern China. *Sci. Rep.* **9**, 2347 (2019), 10.1038/s41598-019-38818-x.
74. T. Caley *et al.*, A two-million-year-long hydroclimatic context for hominin evolution in southeastern Africa. *Nature* **560**, 76–79 (2018).
75. M. H. Simon *et al.*, Eastern South African hydroclimate over the past 270,000 years. *Sci. Rep.* **5**, 18153 (2015), 10.1038/srep18153.
76. R. B. Owen *et al.*, Progressive aridification in East Africa over the last half million years and implications for human evolution. *Proc. Natl. Acad. Sci. U.S.A.* **115**, 11174–11179 (2018).
77. T. C. Johnson *et al.*, A progressively wetter climate in southern East Africa over the past 1.3 million years. *Nature* **537**, 220–224 (2016).
78. S. J. Ivory *et al.*, Environmental change explains cichlid adaptive radiation at Lake Malawi over the past 1.2 million years. *Proc. Natl. Acad. Sci. U.S.A.* **113**, 11895–11900 (2016).
79. R. Grün *et al.*, U-series and ESR analyses of bones and teeth relating to the human burials from Skhul. *J. Hum. Evol.* **49**, 316–334 (2005).
80. D. E. Bar-Yosef Mayer, B. Vandermeersch, O. Bar-Yosef, Shells and ochre in Middle Paleolithic Qafzeh Cave, Israel: Indications for modern behavior. *J. Hum. Evol.* **56**, 307–314 (2009).
81. H. P. Schwarcz *et al.*, ESR dates for the hominid burial site of Qafzeh in Israel. *J. Hum. Evol.* **17**, 733–737 (1988).
82. C. Stringer, The origin and evolution of *Homo sapiens*. *Philos. T. R. Soc. B.* **371**, 20150237 (2016), 10.1098/rstb.2015.0237.
83. M. Martinón-Torres, S. Xing, W. Liu, J.-M. Bermúdez de Castro, A "source and sink" model for East Asia? Preliminary approach through the dental evidence. *C. R. Palevol.* **17**, 33–43 (2018).
84. Y. J. Wang *et al.*, Millennial- and orbital-scale changes in the East Asian monsoon over the past 224,000 years. *Nature* **451**, 1090–1093 (2008).
85. Y. B. Sun *et al.*, Persistent orbital influence on millennial climate variability through the Pleistocene. *Nat. Geosci.* **14**, 812–818 (2021).
86. M. S. Li, L. Hinnov, L. Kump, Acycle: Time-series analysis software for paleoclimate research and education. *Comput. Geosci.* **127**, 12–22 (2019).
87. H. Ao, Z. Zhang, Environmental magnetic data of Asian summer monsoon variability from the Chinese Loess Plateau over the last 280 kyr. East Asian Paleoenvironmental Science Database. https://dx.doi.org/10.12262/IEECAS.EAPSD2023012. Deposited 15 December 2023.